Reaction
Chemistry &
Engineering

ROYAL SOCIETY
OF CHEMISTRY

PAPER

View Article Online
View Journal

Check for updates

Cite this: DOI: 10.1039/d6re00038j

Received 4th February 2026,
Accepted 7th April 2026

DOI: 10.1039/d6re00038j

rsc.li/reaction-engineering

Dual-OSDA ultrafast synthesis of AFX zeolite for enhanced catalytic performance in selective catalytic reduction of NO_x with NH_3

Y. Qin,[a] M. Takemoto,[a] H. Fujinuma,[b] S. P. Elangovan,[b] Y. Yanaba,[c]
T. Okubo[a] and T. Wakihara*[ab]

This paper presents a dual-OSDA approach for the ultrafast synthesis of AFX zeolite, addressing challenges in terms of cost and synthesis efficiency. By partially replacing the expensive organic structure-directing agent, *N*,*N*,*N*′,*N*′-tetraethylbicyclo[2.2.2]oct-7-ene-2,3:5,6-dipyrrolidinium, with a more economical alternative, *viz.*, *N*,*N*′-bis-triethylpentanediyldiammonium dibromide, this method successfully reduces the synthesis cost while maintaining high crystallinity. Compared with the conventionally synthesized samples, the samples synthesized *via* the dual-OSDA method exhibited high hydrothermal stability and excellent catalytic performance in the selective catalytic reduction of NO_x with NH_3 (SCR). Furthermore, employing tubular reactors in the synthesis process facilitated the ultrafast crystallization of AFX zeolite, thus significantly shortening the synthesis time.

1 Introduction

AFX zeolite has garnered increasing attention owing to its distinctive microporous structure comprising 8-membered ring channel systems.[1] The AFX structure belongs to the ABC-6 family of zeolite frameworks and is characterized by an AABBCCBB stacking sequence of 6-ring layers that form *aft* and *gme* cages (see Fig. S1). A microporous material with an AFX structure was first synthesized in the silicoaluminophosphate (SAPO) form, named SAPO-56.[2] In 1993, Zones reported an aluminosilicate form of AFX, known as SSZ-16.[3] AFX zeolite has been extensively investigated for various catalytic applications owing to its favourable pore accessibility. It has been explored in hydrocarbon conversion processes, such as *n*-alkane transformation[4] and methanol-to-olefin/hydrocarbon reactions,[5] as well as in CO_2 hydrogenation to methanol for sustainable fuel production.[6] Additionally, Cu-exchanged AFX zeolites have demonstrated promising potential in the selective catalytic reduction of nitrogen oxides (NO_x) using ammonia (NH_3-SCR), underscoring their applicability in environmental catalysis.[7–10] For instance, Priya *et al.*[11] demonstrated that Cu-exchanged SSZ-16 with an AFX framework exhibited superior NO_x conversion performance in NH_3-SCR compared with other Cu-exchanged zeolites, such as SSZ-13, ZSM-5, and SSZ-39, particularly at elevated temperatures, thus highlighting its thermal stability and catalytic efficiency.

Among the various factors influencing the hydrothermal synthesis of zeolites, structure-directing agents play a decisive role in promoting the crystallization of a specific framework and morphology, thereby favouring the formation of the target phase while minimizing the presence of competing impurity phases.[12] The AFX zeolite was initially synthesized using a heterocyclic compound derived from quinuclidine as the organic structure-directing agent (OSDA), which required 6 days to yield the crystalline product.[3] Since then, various synthesis methods have been developed, which typically require relatively long synthesis periods, ranging from 6 to 21 days.[13,14] The choice of the OSDA determines the practicality of the synthesis process. Though commonly used OSDAs such as 1,1′-(1,4-butanediyl)bis-4-aza-1-azoniabicyclo[2.2.2]octane dibromide (DABCO, see molecular structures in Fig. S2(a)) and *N*,*N*′-bis-triethylpentanediyldiammonium dibromide (Et_6-diquat-5, see molecular structures in Fig. S2(b)) are economical, they often result in prolonged synthesis times. In contrast, more structurally complex OSDAs, such as *N*,*N*,*N*′,*N*′-tetraethylbicyclo[2.2.2]oct-7-ene-2,3:5,6-dipyrrolidinium (TEBOP, see molecular structures in Fig. S2(c)), can significantly reduce crystallization time; however, their higher costs and complicated preparation procedures[15,16] limit the industrial applications of zeolites. Cost estimation based on the synthetic procedures reported in the literature and the corresponding precursor prices (see

---

[a] Department of Chemical System Engineering, The University of Tokyo, 7-3-1 Hongo, Bunkyo-ku, Tokyo 113-8656, Japan. E-mail: wakihara@chemsys.t.u-tokyo.ac.jp
[b] Institute of Engineering Innovation, The University of Tokyo, 2-11-16 Yayoi, Bunkyo-ku, Tokyo 113-8656, Japan
[c] Institute of Industrial Science, The University of Tokyo, 4-6-1 Komaba, Meguro-ku, Tokyo, 153-8505 Japan

synthetic schemes in Fig. S2(d–f) and the detailed catalog price in Table S1) reveals substantial cost differences among the OSDAs. While DABCO and Et_6-diquat-5 are synthesized from inexpensive, commercially available precursors with short reaction times, TEBOP relies on exo-bicyclo[2.2.2]octane tetracarboxylic dianhydride, a highly expensive precursor that results in a precursor cost more than an order of magnitude higher than that of the others. These factors collectively indicate that the synthesis of TEBOP imposes a substantial economic and operational burden.

To address these challenges, the dual-OSDA method offers a cost-effective solution for AFX zeolite synthesis. In this approach, a small amount of an expensive OSDA initiates nucleation, whereas a larger quantity of a cost-effective OSDA enables complete crystallization, thus reducing the overall synthesis cost. Previous studies have proven this dual-OSDA approach to be effective for the cost-efficient synthesis of various zeolites.[17,18] For example, the NU-87 zeolite (NES type) was synthesized by replacing the costly decamethonium bromide with low-cost secondary SDAs, such as 1,3-propanediamine and 1,4-butanediamine, achieving up to 50% substitution without compromising the crystallinity.[19] Nevertheless, to date, no studies have applied the dual-OSDA approach to reduce the consumption of complex OSDAs in AFX synthesis.

Herein, we report a novel and cost-effective dual-OSDA approach for AFX zeolite synthesis, in which TEBOP is partially replaced with the more affordable Et_6-diquat-5. This method minimizes the use of costly OSDAs, thereby effectively reducing synthesis costs while preserving key material properties such as hydrothermal stability. In particular, the dual-OSDA-synthesized AFX zeolite exhibited enhanced activity and stability in NH_3-SCR.

2 Experimental

2.1 Materials

Fumed silica (Aerosil® 200), FAU zeolite (Tosoh; HSZ-350HUA; Si/Al = 5.5), NaOH (FUJIFILM Wako Pure Chemical), $Al(NO_3)_3·9H_2O$ (FUJIFILM Wako Pure Chemical; guaranteed reagent), and 1 M sulfuric acid (H_2SO_4, FUJIFILM Wako Pure Chemical; for volumetric analysis) were used as received. Ammonium nitrate (NH_4NO_3) and copper(II) acetate monohydrate ($Cu(CH_3COO)_2·H_2O$) purchased from FUJIFILM Wako Pure Chemical Corporation were dissolved in deionized water to prepare aqueous solutions for ion-exchange. TEBOP, Et_6-diquat-5, and DABCO were used as the OSDAs for the AFX zeolite synthesis. DABCO, TEBOP and Et_6-diquat-5 were synthesized according to previously reported procedures.[13,20]

2.2 Synthesis of AFX seeds

AFX zeolite seeds were prepared using Et_6-diquat-5 as the OSDA, following a slightly modified procedure based on a previous study.[13] First, deionized water, NaOH solution, Et_6-diquat-5, $Al(NO_3)_3·9H_2O$, and fumed silica were sequentially added to a 50 mL polypropylene bottle in a molar composition of 1 SiO_2 : 0.017 Al_2O_3 : 1 NaOH : 0.1 Et_6-diquat-5 : 40 H_2O. The mixture was stirred at 25 °C and 500 rpm overnight to ensure homogeneity and then transferred into a Teflon-lined stainless-steel autoclave. Crystallization was performed at 150 °C for 7 d. The solid product was recovered through filtration, thoroughly washed with deionized water, and dried at 80 °C overnight. The obtained crystalline zeolite, designated as "AC-E0.1", was used as seeds.

2.3 Acid-leaching of AFX seeds

AC-E0.1 was dispersed in 0.5 M H_2SO_4, and the mixture was stirred for 27 h at 80 °C. The resulting solid was recovered by centrifugation, washed with deionized water, and dried at 80 °C. The obtained zeolite was labelled as "acid-leached seeds".

2.4 Dual-OSDA synthesis of AFX zeolite

For the dual-OSDA synthesis, deionized water, NaOH solution, OSDAs, and FAU zeolites were mixed in a molar composition of 1 SiO_2 : 0.092 Al_2O_3 : 0.25 NaOH : 0.095 OSDA : 30 H_2O. The mixture was stirred at room temperature for 2 h, and the acid-leached seeds were added to the mixture. The final mixture was transferred into an autoclave and heated in an oven at 210 °C. The solid product was collected *via* centrifugation, washed thoroughly with deionized water, and dried at 80 °C overnight. The naming convention for the samples reflects the OSDA/Si ratio in the dual-OSDA system, where T, E, and D represent TEBOP, Et_6-diquat-5, and DABCO, respectively. For instance, the sample labelled T0.024E0.071 indicates an OSDA/Si ratio of 0.024 TEBOP and 0.071 Et_6-diquat-5, corresponding to a system in which 75% of TEBOP in the original recipe was replaced with Et_6-diquat-5. The synthesis procedures for the reference sample, SSZ-13 zeolite (CHA type), are described in the SI.

2.5 Ultrafast synthesis of AFX zeolite

The ultrafast synthesis of AFX was carried out by replacing conventional autoclaves (ACs) with tubular reactors (TRs; Fig. S3) and increasing the temperature from 210 °C to 220 °C. The TR was fabricated from a standard 1/4-inch stainless-steel tube with a length of approximately 13.5 cm, with both ends sealed with standard Swagelok® caps. The sequence of reagent addition and the synthesis procedure remained consistent with those mentioned in section 2.4. The obtained material was designated as TR-T0.024E0.071.

2.6 Hydrothermal stability test

The hydrothermal stability tests were conducted using a custom-built experimental setup. The zeolite samples were packed in the middle zone of a quartz tube and held with glass wool. The samples were then gradually heated to 800 °C for 75 min and treated in air with steam for 7 h. During this process, water was introduced using a syringe pump (Pump

11 Elite, Harvard Apparatus) to maintain a steady water content of 10 vol% under atmospheric pressure. These hydrothermally treated samples are termed "aged".

2.7 Cu ion-exchange

The as-synthesized AFX zeolite samples were calcined at 600 °C for 5 h in dry air at a controlled ramp rate of 1.9 °C min^{-1}. The calcined samples were then ion-exchanged with a 1 M NH_4NO_3 solution to obtain the ammonium-form AFX samples, which were further immersed in a 3 wt% $Cu(CH_3COO)_2 \cdot H_2O$ solution at 90 °C for 2 h. A second calcination step was performed to stabilize the Cu species within the framework. The synthesis procedures for the reference sample, SSZ-13 zeolite (CHA type), are described in the SI.

2.8 NH_3-SCR testing

First, 25 mg of the Cu-exchanged zeolite was packed in a quartz reactor (inner diameter: 4 mm) and held with glass wool. For pretreatment, the reactor was purged with a gas mixture comprising 5% oxygen and 95% nitrogen and then heated to 150 °C. The catalytic performance was evaluated over a temperature range of 150–500 °C, with increments of 50 °C, using a reaction gas mixture containing 300 ppm NO, 300 ppm NH_3, 3% H_2O, 5% O_2, and N_2 as the balance. The total gas flow rate was maintained at 100 $\text{cm}^3\ \text{min}^{-1}$, corresponding to a gas hourly space velocity (GHSV) of $2.08 \times 10^5\ \text{h}^{-1}$.

NO_x conversion was quantified using a chemiluminescent NO_x analyzer (ECL-88A, Yanaco), providing precise catalytic efficiencies under various conditions. The NH_3 concentration was quantified using a laser gas analyzer (LGD F200P2-H, Axetris) based on tunable diode laser spectrometry for selective and accurate detection. Furthermore, the amount of N_2O by-product was quantified using a gas chromatograph (GC-8A, Shimadzu).

The NO_x conversion rate and N_2 selectivity are calculated as follows:

$$\text{No}_x\ \text{conversion} = \left(1 - \frac{[\text{No}_x]_{\text{out}}}{[\text{No}_x]_{\text{in}}}\right) \times 100\%$$

$$N_2\ \text{selectivity} = \frac{[\text{NO}]_{\text{in}} - [\text{NO}]_{\text{out}} + [\text{NH}_3]_{\text{in}} - [\text{NH}_3]_{\text{out}} - [\text{NO}_2]_{\text{out}} - 2[\text{N}_2\text{O}]_{\text{out}}}{[\text{NO}]_{\text{in}} - [\text{NO}]_{\text{out}} + [\text{NH}_3]_{\text{in}} - [\text{NH}_3]_{\text{out}}} \times 100\%$$

2.9 Characterization

Samples were characterized using the powder X-ray diffraction (XRD) technique on a Rigaku Ultima IV diffractometer with CuKα radiation (λ = 1.5406 Å, V = 40 kV, and I = 40 mA) at a 4° min^{-1} scan rate. Crystallinity was evaluated by comparing the integrated peak area between 2θ = 3° and 50° before and after hydrothermal aging. The morphology and particle size were determined using field-emission scanning electron microscopy (FE-SEM; JSM-7000F JEOL, Japan). Solid-state magic-angle spinning nuclear magnetic resonance (MAS NMR) spectroscopy was performed using a JNM-ECA 500 (JEOL) instrument. The spectra were recorded using 49 152 scans to ensure a sufficient signal-to-noise ratio. ^{27}Al MAS NMR measurements were also performed using a custom-built single-tune MAS NMR probe with a 3.2 mm rotor diameter at a high magnetic field strength of 18.79 T, corresponding to an ^{27}Al resonance frequency of 208.49 MHz. N_2 adsorption–desorption measurements were performed using a Quantachrome Autosorb-iQ2 instrument at liquid N_2 temperature. Prior to the measurements, the samples were degassed at 350 °C for 6 h under vacuum. The surface areas were calculated using the multipoint Brunauer–Emmett–Teller (BET) method over a P/P_0 range of 0.05–0.2, and micropore volumes were determined using the t-plot method. Inductively coupled plasma atomic emission spectrometry (ICP-AES; Thermo iCAP 6300) was used to analyze the elemental composition of the samples. UV-vis spectroscopy was performed using a JASCO V-670 spectrophotometer over a wavelength range of 150–400 nm. FT-IR spectra were acquired on a JASCO FT/IR-6600 spectrometer equipped with a mercury cadmium telluride (MCT) detector. Prior to measurement, the samples were activated at 500 °C for 1 h under a nitrogen flow, and the spectra were recorded in diffuse reflectance mode.

3 Results and discussion

Fig. 1 shows the XRD patterns of the AFX samples synthesized using different types of OSDAs. When TEBOP was used as the OSDA, pure AFX zeolite was synthesized within 3 h (Fig. 1(a)). However, when using Et_6-diquat-5 as the OSDA for the synthesis time of 3 h, the XRD pattern exhibited the characteristic peaks corresponding to both FAU and AFX, indicating an intermediate state (Fig. 1(b)). Upon extending the synthesis time to 4 h, the FAU peak intensity decreased, whereas the AFX peaks became stronger, demonstrating the gradual transformation of FAU into AFX.

After 4.5 h, the FAU peaks disappeared completely, indicating a complete phase transition. However, additional peaks at approximately 15.9° and 18.4° were observed, corresponding to ANA-phase impurities. ANA is a common by-product that co-crystallizes during AFX zeolite synthesis, particularly under suboptimal reaction conditions or competing nucleation pathways.[21] Furthermore, AFX crystallization with Et_6-diquat-5 requires a longer synthesis time than with TEBOP, highlighting the relatively weaker structure-directing ability of Et_6-diquat-5. Notably, when DABCO was used (Fig. 1(c)), the XRD patterns displayed strong FAU characteristic peaks with weak AFX signals within 4 h, indicating that DABCO alone provides insufficient structure-directing ability for rapid AFX synthesis. In addition, the effect of increasing Et_6-diquat-5 content or alkalinity on AFX synthesis was evaluated. As shown in Fig. S4(a–c), increasing the Et_6-diquat-5/Si ratio from 0.11 to 0.13

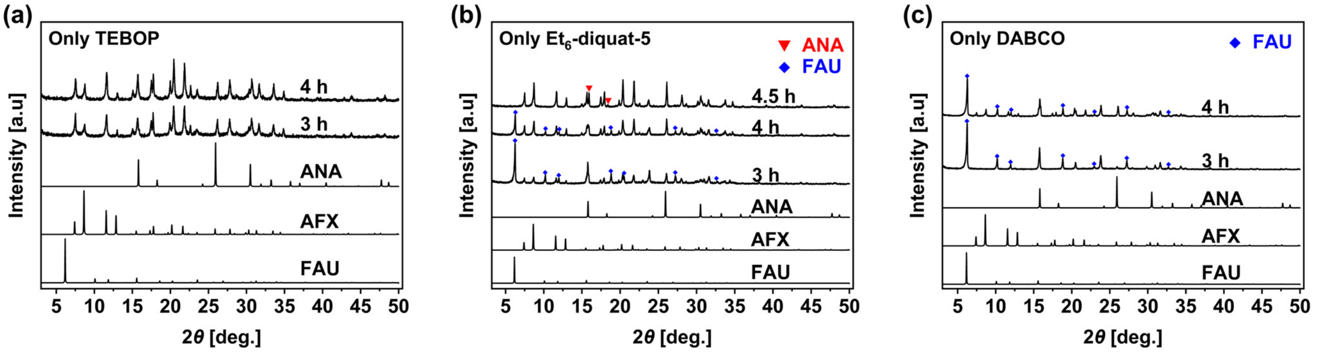

Fig. 1 Powder XRD patterns of the AFX samples synthesized using (a) *N*,*N*,*N*′,*N*′-tetraethylbicyclo[2.2.2]oct-7-ene-2,3:5,6-dipyrrolidinium (TEBOP), (b) *N*,*N*′-bis-triethylpentanediyldiammonium dibromide (Et_6-diquat-5), and (c) 1,1′-(1,4-butanediyl)bis-4-aza-1-azoniabicyclo[2.2.2]octane (DABCO).

did not eliminate ANA impurities, although the AFX crystallization rate was slightly improved. Similarly, increasing the alkalinity failed to completely transform FAU into pure AFX. (Fig. S4(d and e)) These results indicate that neither an excess OSDA nor higher alkalinity is sufficient to achieve pure AFX synthesis using Et_6-diquat-5. Nonetheless, Et_6-diquat-5 remains a viable OSDA for AFX zeolite synthesis, achieving the desired phase within a few hours, albeit with ANA impurities. This underscores the potential of a dual-OSDA approach combining both TEBOP and Et_6-diquat-5 to enhance synthesis efficiency and mitigate the formation of undesired phases. Conversely, DABCO is unsuitable for the ultrafast synthesis of AFX, as the resulting AFX zeolite exhibits inferior hydrothermal stability compared to that synthesized with TEBOP, making it less suitable for catalytic applications.[16]

To investigate the potential of the dual-OSDA approach and gain deeper insight into the roles of different OSDAs, 50% of TEBOP in the previously mentioned recipe was substituted with either Et_6-diquat-5 or DABCO. (TEBOP/Si = 0.0475; Et_6-diquat-5 or DABCO/Si = 0.0475) As depicted in Fig. 2(a and b), with a 50% reduction in TEBOP, the synthesis successfully yielded fully crystallized pure AFX zeolite within 4 h. This indicates that the TEBOP concentration can be reduced without compromising the structural integrity or synthesis rate of AFX zeolite.

To emphasize the role of Et_6-diquat-5 in the dual-OSDA method, two synthesis conditions were compared: (1) replacing 75% of TEBOP with Et_6-diquat-5 to achieve a total OSDA composition of 0.024 TEBOP and 0.071 Et_6-diquat-5 (denoted as AC-T0.024E0.071) and (2) reducing the TEBOP amount to 25% of its original quantity without adding Et_6-diquat-5 (AC-T0.024). Both syntheses were conducted at 210 °C for 4 h. The resulting samples were characterized using XRD and SEM. The XRD patterns confirmed that the dual-OSDA sample (AC-T0.024E0.071) formed a pure AFX phase, whereas the low-TEBOP-only system (AC-T0.024) contained ANA impurities (Fig. 3(a)). Fig. 3(b) and (c) show the morphologies of AC-T0.024E0.071 and AC-T0.024, respectively. The small crystals (100–300 nm) and the larger spherical crystals (2–3 μm) correspond to AFX and ANA zeolites, respectively. This further validates that the dual-OSDA approach promotes the formation of pure AFX zeolite with uniform crystal size, whereas low-content TEBOP alone leads to ANA impurities.

Compared with the conventionally synthesized AFX seeds (AC-E0.1; Fig. 3(d)), which typically exhibit crystal sizes in the 2–4 μm range, the dual-OSDA-synthesized samples exhibit significantly smaller crystal sizes. This reduction in particle size may enhance the accessibility of active sites and improve the mass transfer efficiency, both of which are critical for enhancing catalytic performance in NH_3-SCR. A smaller particle size would also enable a more uniform dispersion of the Cu species during ion exchange, thereby improving the accessibility and density of the Cu active

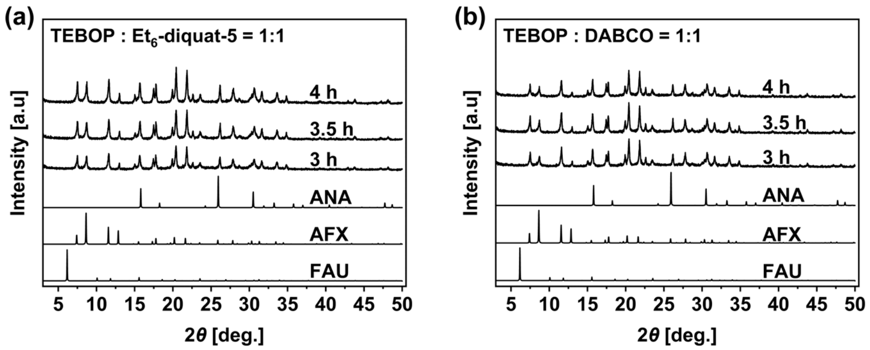

Fig. 2 Powder XRD patterns of AFX samples synthesized using dual OSDAs of (a) TEBOP and Et_6-diquat-5 and (b) TEBOP and DABCO.

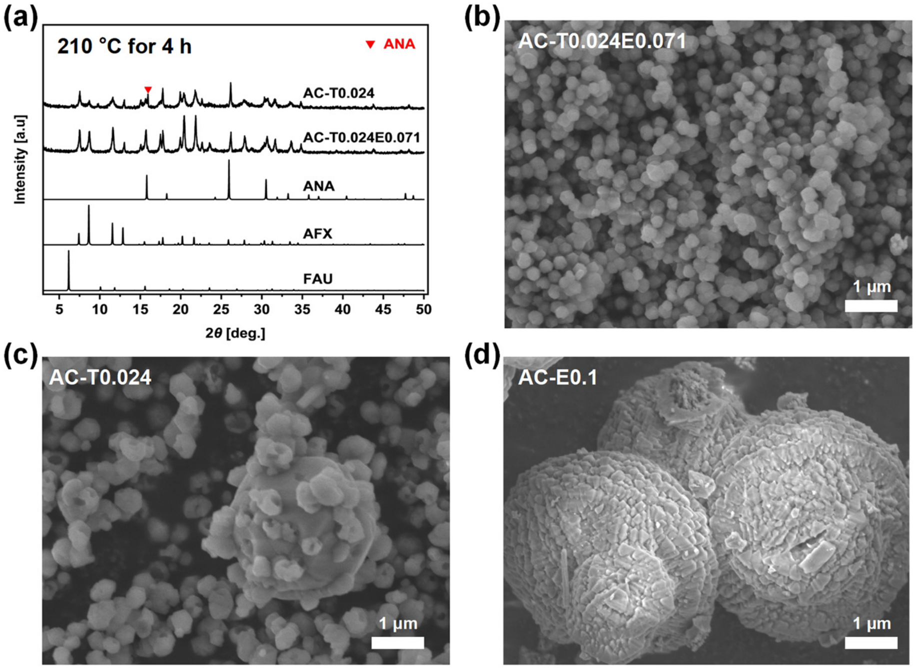

Fig. 3 (a) XRD patterns of AFX samples synthesized using the dual-OSDA method; SEM images of AFX samples synthesized using (b) the dual-OSDA method involving 0.024 TEBOP and 0.071 Et_6-diquat-5, (c) 0.024 TEBOP alone, and (d) the conventional method involving Et_6-diquat-5.

sites, ultimately leading to improved catalytic performance especially at high temperatures.[22,23]

Fig. 4 demonstrates ^{13}C CP MAS NMR spectra of samples synthesized with different proportions of organic structure-directing agents. A distinct peak at approximately 20 ppm was observed in the samples synthesized using Et_6-diquat-5 (AC-E0.1) alone and a combination of 25% TEBOP and 75% Et_6-diquat-5 (AC-T0.024E0.071). This peak corresponds to the central methylene carbon (C1) in the Et_6-diquat-5 structure, which bridged the two quaternary ammonium groups. However, this peak was absent in AC-T0.0475E0.0475, in which 50% of TEBOP was substituted with Et_6-diquat-5. This suggests that TEBOP alone was sufficient to direct AFX crystallization even at half of its original amount. Similarly, when 50% of TEBOP was replaced with DABCO, DABCO neither participated in the crystallization nor became incorporated into the framework. As a result, the NMR spectrum of the obtained sample (AC-T0.0475D0.0475) was

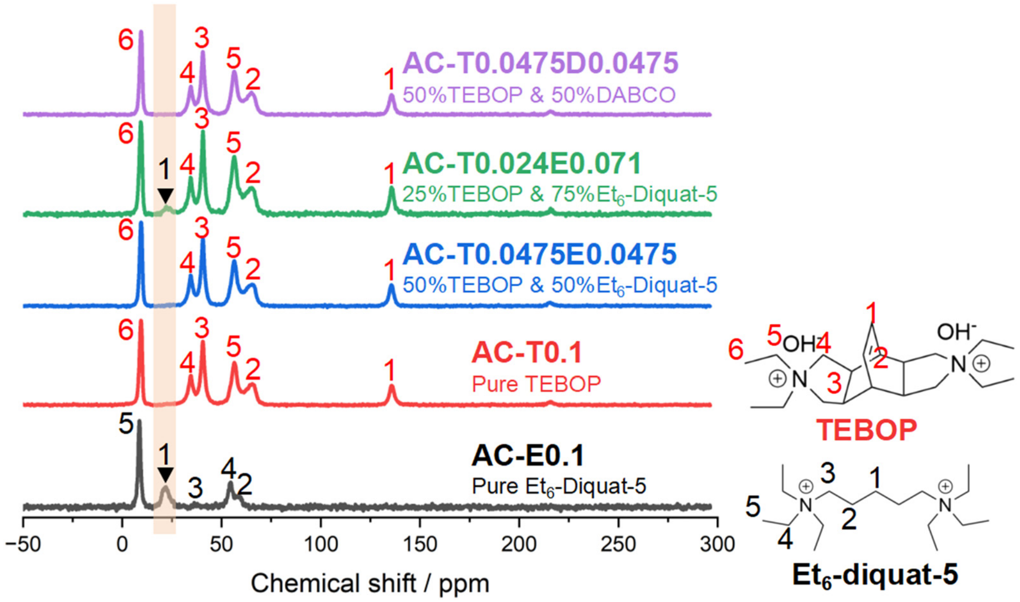

Fig. 4 ^{13}C CP MAS NMR spectra of AFX samples synthesized with different proportions of organic structure-directing agents.

identical to that synthesized solely with TEBOP (AC-T0.1), showing no characteristic peaks attributable to DABCO.

Nevertheless, when the TEBOP content was further reduced to 25% (AC-T0.024E0.071), a characteristic peak associated with Et_6-diquat-5 appeared, contributing to its active participation in the structure-directing process and the successful crystallization of pure AFX. These findings strongly suggest that Et_6-diquat-5 becomes essential only when TEBOP is insufficient to promote independent AFX formation. Notably, although TEBOP plays a dominant role in AFX synthesis, Et_6-diquat-5 can also contribute to crystallization under appropriate conditions by integrating into the framework. Moreover, as previously discussed, Et_6-diquat-5 alone resulted in a slower crystallization rate and ANA impurities, in contrast to TEBOP alone. However, the dual-OSDA approach maintained the crystallization rate and yielded fully crystallized AFX within 4 h. These results demonstrate the potential of the dual-OSDA method for synthesizing pure AFX without compromising crystallization efficiency.

Ultrafast synthesis of AFX was performed in a tubular reactor and an oil bath, which eliminated the thermal lag commonly observed in conventional ACs, thereby significantly enhancing heat transfer efficiency.[24] Rapid heating is crucial for preventing OSDA decomposition, seed dissolution, and the formation of undesirable phases. In addition, crystallization is favoured at elevated temperatures, allowing for faster and more controlled crystal growth.[25] Several recent studies have reported the ultrafast synthesis of AFX zeolites over several hours or within minutes. For example, Chokkalingam *et al.* achieved a highly crystalline AFX zeolite within 2 h using TEBOP in a TR.[16] Yoshioka *et al.* further advanced this field by developing an ultrafast synthesis route that produced highly crystalline AFX zeolites in 12 min.[15] Despite these advancements, ultrafast synthesis of AFX still relies on TEBOP.

Ultrafast synthesis using tubular reactors has proven to significantly reduce reaction times from several days to hours or even minutes, as demonstrated by previous studies.[26–30] Building upon the established research, this study optimizes the synthesis conditions to realize ultrafast synthesis using a TR instead of a conventional AC, improving efficiency and reducing costs. To evaluate the effect of precursor aging on the crystallization process, synthesis was performed with an extended aging period of 18 h at 90 °C. As illustrated in Fig. 5(a), pure AFX zeolite was synthesized at 210 °C within 50 min. Increasing the temperature to 220 °C further reduced the synthesis time to only 40 min. Additionally, Fig. 5(b) shows that aging the precursor mixture at 90 °C for 18 h significantly accelerated crystallization, forming pure AFX in only 30 min at 210 °C and 20 min at 220 °C. This is attributed to the formation of an initial aluminosilicate species during aging, which enables the rapid synthesis of highly crystallized AFX zeolites within reduced timeframes. These findings suggest that the dual-OSDA method is well suited for ultrafast AFX synthesis at higher temperatures and highlights its potential for scalable, cost-effective continuous flow synthesis for industrial application.

In practical applications, such as the periodic regeneration of upstream diesel particulate filter modules using water from diesel engine exhaust, the operating temperature of the Cu-based SCR catalysts must demonstrate resistance to hydrothermal aging[31–35] To evaluate this, all samples were tested for NH_3-SCR performance before and after hydrothermal aging at 800 °C. Fig. 6(a) and (b) present a comparison of the catalytic performances of fresh and aged AFX zeolites synthesized *via* different methods against Cu-SSZ-13 (CHA-type, Si/Al = 4.0), which was the most comprehensively studied SCR catalyst and chosen as a benchmark SCR catalyst. Compared to Cu-SSZ-13, all fresh AFX samples exhibited excellent NO_x conversion (>90%) over a wide temperature range of 150–400 °C (Fig. 6(a)). Notably,

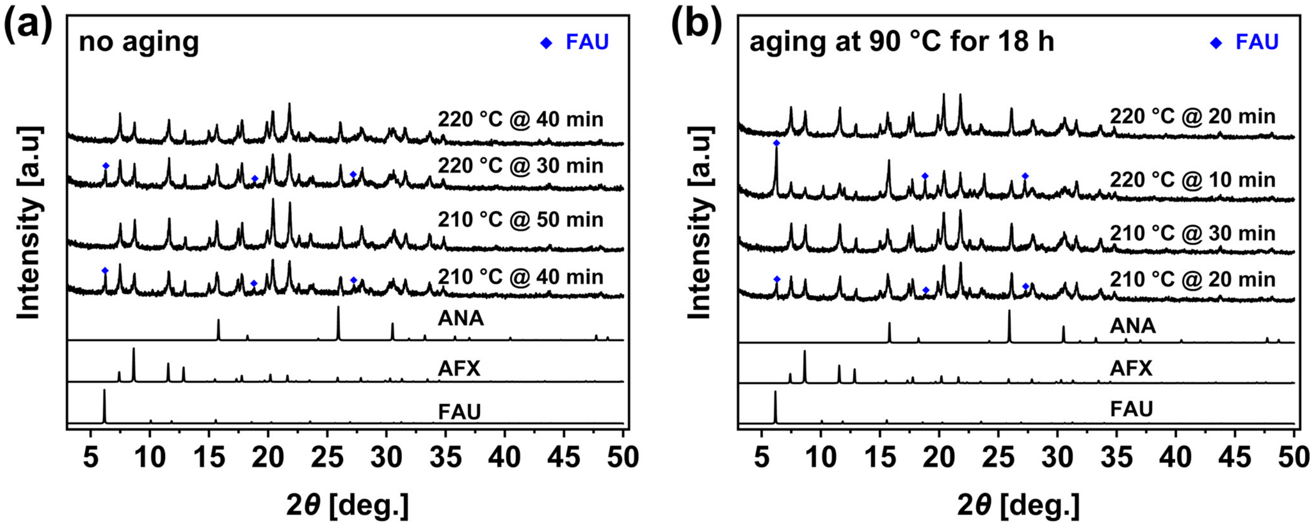

Fig. 5 XRD patterns of ultrafast and dual-OSDA-synthesized AFX zeolites under different aging conditions: (a) room temperature for 2 h and (b) 90 °C for 18 h.

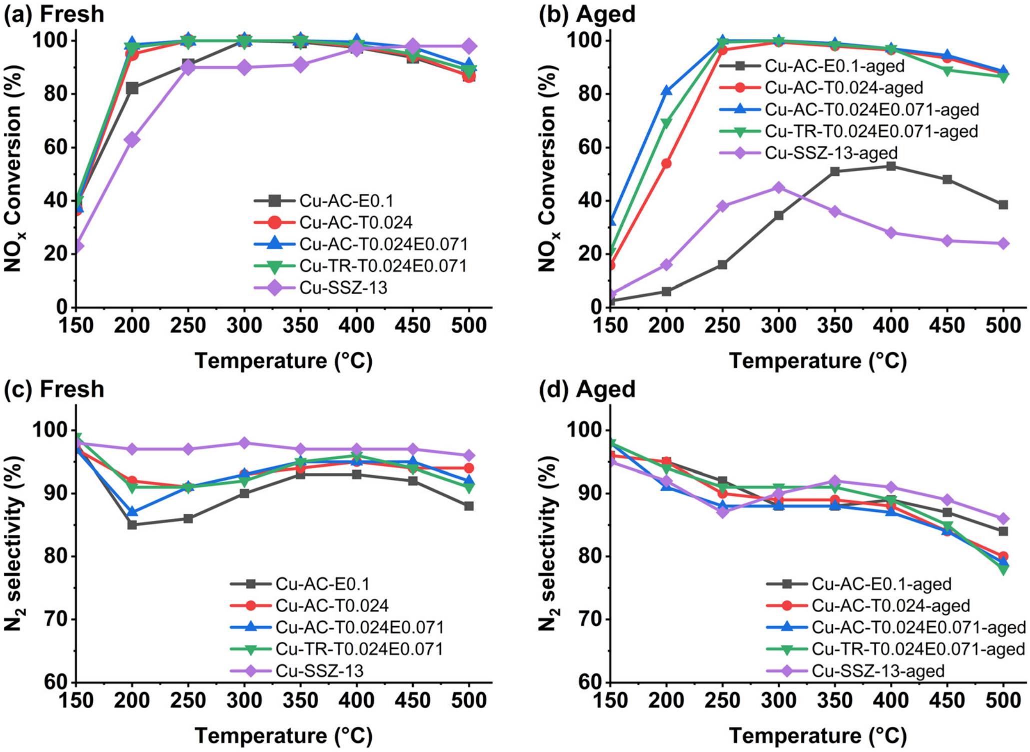

Fig. 6 NO$_x$ conversion during NH$_3$-SCR using (a) fresh and (b) aged AFX zeolites and the Cu-SSZ-13 zeolite at 800 °C for 7 h in 10 vol% steam; N$_2$ selectivity during NH$_3$-SCR of (c) fresh and (d) aged AFX samples and the Cu-SSZ-13 zeolite at 800 °C for 7 h in 10 vol% steam.

the dual-OSDA sample (Cu-AC-T0.024E0.071) exhibited catalytic activity comparable to that of the conventional sample (Cu-AC-E0.1), demonstrating the effectiveness of the dual-OSDA approach. In fact, at lower temperatures (~200 °C), Cu-AC-T0.024E0.071 exhibited slightly better NO$_x$ conversion than Cu-AC-T0.024. The NO$_x$ conversion rate of aged Cu-AC-T0.024E0.071 decreased notably at 200 °C but rapidly rose to nearly 100% at 250 °C and remained above 80% up to 500 °C (Fig. 6(b)). In contrast, the aged Cu-AC-E0.1 exhibited a maximum NO$_x$ conversion of <60%, whereas the aged Cu-SSZ-13 catalyst showed a maximum NO$_x$ conversion of only 45%. Cu-AC-T0.024 exhibited poorer catalytic performance than Cu-AC-T0.024E0.071 owing to the presence of ANA impurities, which are absent in the dual-OSDA samples (Fig. 3(a)). All AFX samples, regardless of hydrothermal aging, demonstrated high N$_2$ selectivity (>80%) over the entire temperature range in NH$_3$-SCR, confirming their high selectivity toward the desired product (Fig. 6(c and d)). Although the fresh AFX samples exhibit slightly lower yet acceptable N$_2$ selectivity than Cu-SSZ-13, the aged samples show comparable N$_2$ selectivity to that of aged Cu-SSZ-13. These results evidenced that the dual-OSDA approach does not compromise the product selectivity even after harsh hydrothermal treatment.

Table 1 summarizes the Si/Al ratio, Cu loading, and Cu/Al ratio of the tested AFX samples. The Si/Al ratio of Cu-AC-T0.024E0.071 was approximately 3.4, which is comparable to that of Cu-AC-E0.1 (Si/Al = 3.6). Under the same Cu-ion exchange conditions, Cu-AC-T0.024E0.071 and Cu-TR-T0.024E0.071 achieved a higher Cu loading than Cu-AC-E0.1, which may have contributed to their improved NH$_3$-SCR activity. Cu-AC-E0.1 showed a significant loss of crystallinity after the aging, whereas the aged Cu-AC-T0.024E0.071 retained a higher crystallinity than aged Cu-AC-E0.1 (Fig. 7(a and b)). For Cu-TR-T0.024E0.071, no obvious changes in particle size or morphology were observed in the SEM images. (Fig. S5(a and b)). Degradation of the micropore structure of the tested samples was also confirmed by N$_2$ adsorption–desorption analysis (Table S2). Cu-TR-T0.024E0.071 exhibited similar characteristics to Cu-AC-T0.024E0.071 both before and after aging.

The UV-vis spectra revealed the presence of CuO aggregation in both the fresh and aged Cu-AC-E0.1, as indicated by the broad absorption band in the 200–250 nm range. All samples exhibited comparable absorption at approximately 200 nm, which correspond to the isolated Cu^{2+}/Cu^{+} species.[10] The dual-OSDA samples exhibited only minor CuO-related absorption after hydrothermal aging, suggesting a better dispersion of the Cu species and

Table 1 ICP-AES results of Cu-exchanged AFX catalysts before hydrothermal treatment

Sample name	Si/Al	Cu wt%	Cu/Al
Cu-AC-T0.024	3.9	4.4	0.21
Cu-AC-E0.1	3.6	3.6	0.19
Cu-AC-T0.024E0.071	3.4	4.7	0.21
TR-AC-T0.024E0.071	4.9	4.1	0.24

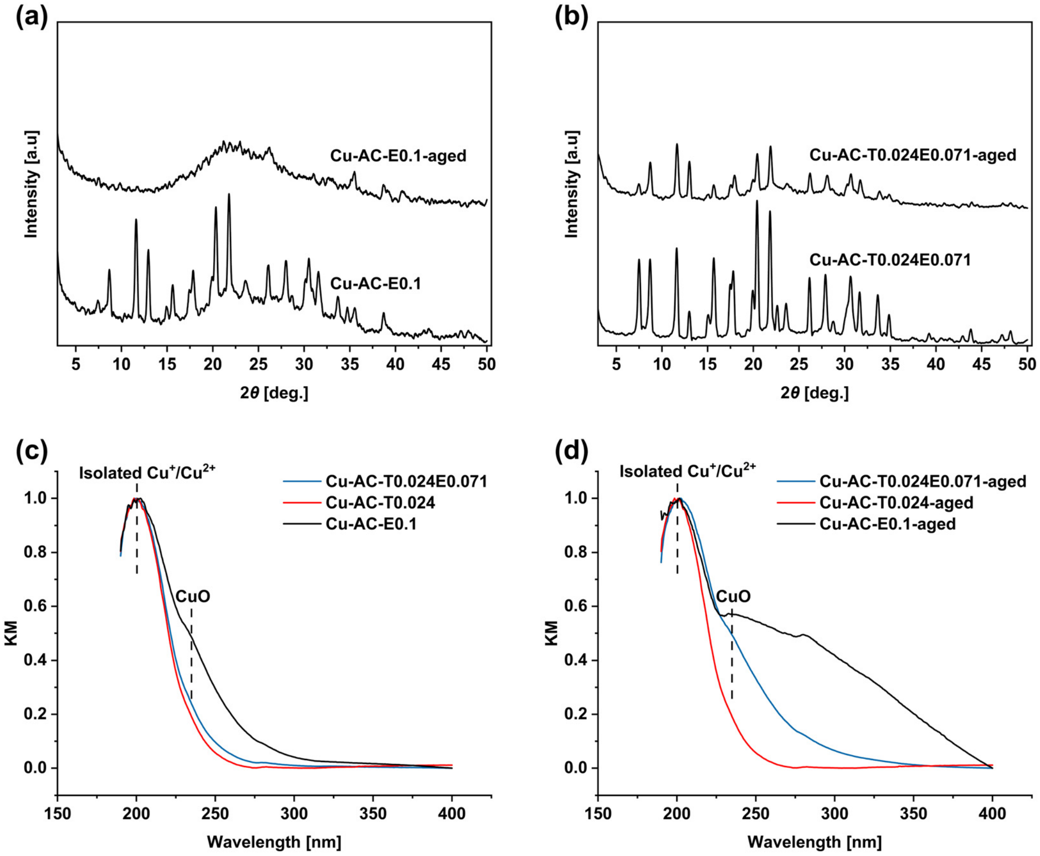

Fig. 7 XRD patterns of (a) Cu-AC-E0.1 and (b) Cu-AC-T0.024E0.071 before and after hydrothermal aging; UV-vis spectra of the AFX zeolite samples (c) before and (d) after hydrothermal aging.

improved framework stability (Fig. 7(c and d)). However, the poor catalytic performance of Cu-AC-E0.1 after hydrothermal aging was not solely due to its lower Cu content but also to its limited hydrothermal stability, which resulted in significant structural degradation under harsh conditions. As reported by M. Ogura *et al.*,[7] rigid OSDAs such as TEBOP^{2+} fit tightly within the *aft* cage, leaving almost no space for additional Na^{+} insertion. This framework keeps the Al atoms apart, thus enhancing the structural stability. In contrast, more flexible OSDAs such as [Dab-4]$^{2+}$ allow the incorporation of additional charge-compensating cations within or between cages, promoting close location of Al and resulting in a less stable framework under hydrothermal conditions.

This structural insight may explain the differences in aging resistance among the samples synthesized using different OSDA combinations. Herein, Et$_6$-Diquat-5 (Fig. S2(b)) exhibited greater molecular flexibility than TEBOP (Fig. S2(c)), which may facilitate the close proximity of the Al atoms in the framework, potentially reducing hydrothermal stability.

^{27}Al MAS NMR characterization was also conducted on both the fresh and aged samples (Fig. S6). Compared with the other samples, Cu-AC-E0.1 did not exhibit a significantly higher amount of extra-framework aluminium (EFAL, typically appearing near 0 ppm) in the fresh state. However, after aging, the resonance of tetrahedrally coordinated framework Al at ~55 ppm almost completely disappeared, indicating severe structural collapse. In contrast, the dual-OSDA sample (aged Cu-AC-T0.024E0.071) retained its structural integrity, with the EFAL signal disappearing after aging. Although the EFAL signal vanished, the overall Si/Al ratio remained almost unchanged. This suggests that the EFAL species may have reintegrated into the zeolite framework.

In addition to the Cu-exchanged zeolites, the hydrothermal stability of the H-form zeolites was evaluated. The XRD patterns (Fig. 8(a)) indicated that H-AC-E0.1 retained only 30% of its relative crystallinity, whereas the aged H-AC-T0.024 E0.071 retained approximately 53%. In contrast, aged H-AC-T0.024 retained only 14% crystallinity, indicating severe structural degradation. These results suggest the superior hydrothermal stability of the aged H-AC-T0.024E0.071 compared with the other samples. Furthermore, FT- IR analysis (Fig. 8(b)) revealed a strong absorption at 3450 cm^{-1} in H-AC-T0.024, indicating the presence of abundant hydrogen-bonded OH groups associated with silanol defects. The peaks at 3740, 3665, and 3450 cm^{-1} correspond to the silanol groups, OH groups from partially truncated Al species

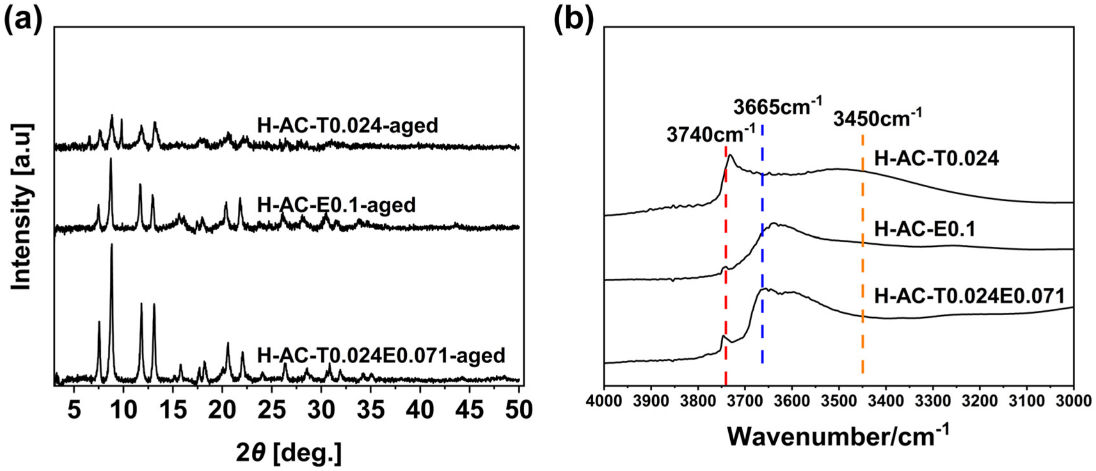

Fig. 8 (a) XRD patterns of H-form AFX samples after hydrothermal aging and (b) FT-IR patterns of H-form AFX samples before hydrothermal aging.

within the framework, and hydrogen-bonded OH groups, respectively.[36] These results suggest that the severe framework deterioration in H-AC-T0.024 under hydrothermal aging is caused by the presence of more silanol defects compared with the other samples.

4 Conclusions

AFX zeolites were synthesized using a dual-OSDA approach, in which the expensive OSDA, TEBOP, was partially replaced with a more cost-effective alternative such as Et_6-diquat-5. This approach effectively lowered the synthesis costs while maintaining high crystallinity, making it a viable method for scalable AFX zeolite production. Compared with conventionally synthesized AFX zeolites, the dual-OSDA samples exhibited smaller particle sizes (100–300 nm). After Cu-ion exchange, the dual-OSDA-synthesized Cu-AFX catalysts demonstrated superior NH_3-SCR performance, achieving over 80% NO_x conversion over the 250–500 °C range, even after hydrothermal aging at 800 °C. Furthermore, the BET surface area and micropore volume measurements confirmed the high structural stability of Cu-AC-T0.024E0.071. XRD and ^{27}Al MAS NMR characterization revealed that Cu-AC-E0.1 underwent structural collapse, whereas Cu-AC-T0.024E0.071 maintained high crystallinity. The observed reduction in EFAL further suggested enhanced framework stability of the dual-OSDA samples. Moreover, by combining TRs with optimized synthesis temperature and aging conditions, the crystallization of AFX zeolites was completed within 20 minutes, achieving significant time reduction while maintaining phase purity. This method also eliminated thermal lag and enhanced heat transfer efficiency, demonstrating its potential for continuous-flow synthesis. Overall, the dual-OSDA approach provides a cost-effective and scalable route for AFX zeolite synthesis, balancing synthesis efficiency, structural integrity, and catalytic performance. Its superior hydrothermal stability highlights its feasibility for practical NO_x reduction applications, paving the way for further optimization and industrial implementation.

Conflicts of interest

The authors declare no conflicts of interest.

Data availability

All data needed to evaluate the conclusions in the paper are present in the paper and/or the supplementary information (SI). Additional data that support the findings of this study are available from the corresponding author upon reasonable request. Supplementary information is available. See DOI: https://doi.org/10.1039/d6re00038j.

Acknowledgements

This work was partly supported by the New Energy and Industrial Technology Development Organization (NEDO) Moonshot Research and Development Program; the Japan Society for the Promotion of Science (JSPS) KAKENHI Grant-in-Aid for Transformative Research Areas (A) (JP20A206 and JP20H05880) and Grant-in-Aid for Scientific Research (S) (JP21H05011 and JP23H05454); and the Materials Processing Science Project ("Materialize") of the Ministry of Education, Culture, Sports, Science and Technology (MEXT) (JPMXP0219192801).

Notes and references

1 M. Dusselier and M. E. Davis, *Chem. Rev.*, 2018, **118**, 5265–5329.
2 S. T. Wilson, R. W. Broach, C. S. Blackwell, C. A. Bateman, N. K. McGuire and R. M. Kirchner, *Microporous Mesoporous Mater.*, 1999, **28**, 125–137.
3 S. I. Zones, *U.S. Pat.*, 5194235, 1993.

4 T. L. M. Maesen, E. Beerdsen, S. Calero, D. Dubbeldam and B. Smit, *J. Catal.*, 2006, **237**, 278–290.

5 G. Sastre, *Catal. Today*, 2014, **226**, 25–36.

6 M. Xiang, Z. Shi, X. Zhang, Z. Gao, J. Guo, Z. Wu, S. Ma, J. Bai, W. Zhang, Y. Deng, J. Zhou and Y. Su, *Fuel*, 2024, **361**, 130663.

7 M. Ogura, Y. Shimada, T. Ohnishi, N. Nakazawa, Y. Kubota, T. Yokoi, M. Ehara, K. Shimizu and N. Tsunoji, *Catalysts*, 2021, **11**, 163.

8 S. Han, W. Rao, J. Hu, X. Tang, Y. Ma, J. Du, Z. Liu, Q. Wu, Y. Ma, X. Meng, W. Shan, F. S. Xiao and H. He, *Appl. Catal., B*, 2023, **332**, 122746.

9 D. W. Fickel, E. D'Addio, J. A. Lauterbach and R. F. Lobo, *Appl. Catal., B*, 2011, **102**, 441–448.

10 A. Palčić, P. C. Bruzzese, K. Pyra, M. Bertmer, K. Góra-Marek, D. Poppitz, A. Pöppl, R. Gläser and M. Jabłońska, *Catalysts*, 2020, **10**, 506.

11 S. V. Priya, T. Ohnishi, Y. Shimada, Y. Kubota, T. Masuda, Y. Nakasaka, M. Matsukata, K. Itabashi, T. Okubo, T. Sano, N. Tsunoji, T. Yokoi and M. Ogura, *Bull. Chem. Soc. Jpn.*, 2018, **91**, 355–361.

12 T. Ikuno, W. Chaikittisilp, Z. Liu, T. Iida, Y. Yanaba, T. Yoshikawa, S. Kohara, T. Wakihara and T. Okubo, *J. Am. Chem. Soc.*, 2015, **137**, 14533–14544.

13 S. H. Lee, C. H. Shin, G. J. Choi, T. J. Park, I. S. Nam, B. Han and S. B. Hong, *Microporous Mesoporous Mater.*, 2003, **60**, 237–249.

14 Y. Bhawe, M. Moliner-Marin, J. D. Lunn, Y. Liu, A. Malek and M. Davis, *ACS Catal.*, 2012, **2**, 2490–2495.

15 T. Yoshioka, Z. Liu, K. Iyoki, A. Chokkalingam, Y. Yonezawa, Y. Hotta, R. Ohnishi, T. Matsuo, Y. Yanaba, K. Ohara, T. Takewaki, T. Sano, T. Okubo and T. Wakihara, *React. Chem. Eng.*, 2021, **6**, 74–81.

16 A. Chokkalingam, W. Chaikittisilp, K. Iyoki, S. H. Keoh, Y. Yanaba, T. Yoshikawa, T. Kusamoto, T. Okubo and T. Wakihara, *RSC Adv.*, 2019, **9**, 16790–16796.

17 A. Javdani, J. Bae, G. Ivanushkin and M. Dusselier, *Mater. Horiz.*, 2025, **12**, 4496–4509.

18 J. Xie, L. Chen, W. H. Wang, P. Wang, C. T. Au and S. F. Yin, *Catal. Sci. Technol.*, 2017, **7**, 1211–1216.

19 W. Shang, P. Li, W. Dai, G. Wu, N. Guan and L. Li, *ChemistrySelect*, 2021, **6**, 3952–3957.

20 S. Inagaki, Y. Tsuboi, Y. Nishita, T. Syahylah, T. Wakihara and Y. Kubota, *Chem. – Eur. J.*, 2013, **19**, 7780–7786.

21 E. Mitani, Y. Yamasaki, N. Tsunoji, M. Sadakane and T. Sano, *Microporous Mesoporous Mater.*, 2018, **267**, 192–197.

22 Y. Li, T. Du, C. Chen, H. Jia, J. Sun, X. Fang, Y. Wang and H. Na, *J. Environ. Chem. Eng.*, 2024, **12**, 111856.

23 M. Cai, A. Palčić, V. Subramanian, S. Moldovan, O. Ersen, V. Valtchev, V. V. Ordomsky and A. Y. Khodakov, *J. Catal.*, 2016, **338**, 227–238.

24 Z. Liu, T. Wakihara, D. Nishioka, K. Oshima, T. Takewaki and T. Okubo, *Chem. Commun.*, 2526, **50**, 28.

25 Z. Liu, J. Zhu, T. Wakihara and T. Okubo, *Inorg. Chem. Front.*, 2019, **6**, 14.

26 A. Chokkalingam, K. Iyoki, N. Hoshikawa, H. Onozuka, W. Chaikittisilp, S. Tsutsuminai, T. Takewaki, T. Wakihara and T. Okubo, *React. Chem. Eng.*, 2020, **5**, 2260.

27 Z. Liu, T. Wakihara, K. Oshima, D. Nishioka, Y. Hotta, S. P. Elangovan, Y. Yanaba, T. Yoshikawa, W. Chaikittisilp, T. Matsuo, T. Akahiko Takewaki and T. Okubo, *Am. Ethnol.*, 2015, **127**, 5775–5779.

28 Z. Liu, T. Wakihara, D. Nishioka, K. Oshima, T. Takewaki and T. Okubo, *Chem. Mater.*, 2014, **26**, 2327–2331.

29 Z. Liu, T. Wakihara, C. Anand, S. H. Keoh, D. Nishioka, Y. Hotta, T. Matsuo, T. Takewaki and T. Okubo, *Microporous Mesoporous Mater.*, 2016, **223**, 140–144.

30 Z. Liu, K. Okabe, C. Anand, Y. Yonezawa, J. Zhu, H. Yamada, A. Endo, Y. Yanaba, T. Yoshikawa, K. Ohara, T. Okubo and T. Wakihara, *Proc. Natl. Acad. Sci. U. S. A.*, 2016, **113**, 14267–14271.

31 R. Li, X. Jiang, J. Lin, Z. Zhang, Q. Huang, G. Fu, Y. Zhu and J. Jiang, *Chem. Eng. J.*, 2022, **441**, 136021.

32 P. N. R. Vennestrøm, T. V. W. Janssens, A. Kustov, M. Grill, A. Puig-Molina, L. F. Lundegaard, R. R. Tiruvalam, P. Concepción and A. Corma, *J. Catal.*, 2014, **309**, 477–490.

33 Y. Shan, J. Du, Y. Yu, W. Shan, X. Shi and H. He, *Appl. Catal., B*, 2020, **266**, 118655.

34 W. Su, Z. Li, Y. Peng and J. Li, *Phys. Chem. Chem. Phys.*, 2015, **17**, 29142–29149.

35 Y. Liang, R. Li, R. Liang, Z. Li, X. Jiang and J. Jiang, *Catalysts*, 2023, **13**, 742.

36 K. Iyoki, K. Kikumasa, T. Onishi, Y. Yonezawa, A. Chokkalingam, Y. Yanaba, T. Matsumoto, R. Osuga, S. P. Elangovan, J. N. Kondo, A. Endo, T. Okubo and T. Wakihara, *J. Am. Chem. Soc.*, 2020, **142**, 3931–3938.